

See discussions, stats, and author profiles for this publication at: <https://www.researchgate.net/publication/257347927>

The autofocusing system of the IMAT neutron camera

Article in *The Review of scientific instruments* · September 2013

DOI: 10.1063/1.4819793 · Source: PubMed

CITATIONS

18

READS

502

6 authors, including:



Francesco Aliotta

Italian National Research Council

139 PUBLICATIONS 1,701 CITATIONS

[SEE PROFILE](#)



Dario Tresoldi

Italian National Research Council

7 PUBLICATIONS 73 CITATIONS

[SEE PROFILE](#)



Rosa C. Ponterio

Italian National Research Council

134 PUBLICATIONS 1,237 CITATIONS

[SEE PROFILE](#)



Cirino Vasi

Italian National Research Council

187 PUBLICATIONS 2,616 CITATIONS

[SEE PROFILE](#)

Some of the authors of this publication are also working on these related projects:



Experimental and theoretical aspects of electrospray and its application for thin film deposition [View project](#)



PANAREA CNR Project in collaboration with STFC [View project](#)

The autofocusing system of the IMAT neutron camera

V. Finocchiaro, F. Aliotta, D. Tresoldi, R. C. Ponterio, C. S. Vasi et al.

Citation: *Rev. Sci. Instrum.* **84**, 093701 (2013); doi: 10.1063/1.4819793

View online: <http://dx.doi.org/10.1063/1.4819793>

View Table of Contents: <http://rsi.aip.org/resource/1/RSINAK/v84/i9>

Published by the AIP Publishing LLC.

Additional information on Rev. Sci. Instrum.

Journal Homepage: <http://rsi.aip.org>

Journal Information: http://rsi.aip.org/about/about_the_journal

Top downloads: http://rsi.aip.org/features/most_downloaded

Information for Authors: <http://rsi.aip.org/authors>

ADVERTISEMENT

For all your variable temperature, solid state characterization needs....
... delivering state-of-the-art in technology and proven system solutions for over 30 years!

MMR TECHNOLOGIES

Seebeck Measurement Systems
Solutions for Optical Setups!

Variable Temperature Microprobe Systems

Hall Measurement Systems

Email: sales@mmr-tech.com Web: www.mmr-tech.com Phone: (650) 962-9622 Fax: (888) 522-1011

The autofocusing system of the IMAT neutron camera

V. Finocchiaro,^{1,2} F. Aliotta,² D. Tresoldi,² R. C. Ponterio,² C. S. Vasi,² and G. Salvato^{2,a)}

¹*Dipartimento di Ingegneria Elettronica, Chimica e Ingegneria Industriale dell'Università di Messina, Contrada di Dio, I-98166 Messina, Italy*

²*CNR-IPCF, Istituto per i Processi Chimico-Fisici, Viale F. Stagno d'Alcontres 37, I-98158 Messina, Italy*

(Received 21 May 2013; accepted 15 August 2013; published online 5 September 2013)

In this paper, we present the autofocusing system of the imaging instrument to be used on IMAT, a new neutron-imaging facility under construction at the ISIS (UK) target station 2. We have compared 16 different autofocus algorithms to select the one with the best performance. The algorithms have been evaluated by using both a qualitative analysis and a quantitative one. An overall score has been computed and the “contrast based” algorithm has been selected for the autofocusing system. The adopted setup together with the described autofocusing system makes the camera a user-friendly imaging device allowing the optimization of beam time use. © 2013 AIP Publishing LLC. [<http://dx.doi.org/10.1063/1.4819793>]

I. INTRODUCTION

The neutron imaging is an emerging, non-destructive, investigation technique with applications in several research fields, such as archaeology, biology, engineering.^{1–6} Neutrons allow radiography and tomography of samples not accessible to x rays. The quality of the obtained images depends on several factors, such as source brilliance, resolution of the camera, scintillator thickness, sample to scintillator distance, and focusing accuracy. This last represents a crucial point: an inaccurate focusing procedure will produce blurred images lowering the effective spatial resolution. The focusing procedure is a mandatory task at any change of the scintillator screen or of the lens. In addition, the adoption of an autofocusing procedure carries the advantage of reducing the needs for accessing areas close to activated items. More generally, it reduces the user intervention, making the device more user-friendly and safe from human errors.

This paper presents the autofocusing system that will be used on IMAT, the new beamline dedicated to neutron imaging and diffraction which is under construction at the Target Station 2 of ISIS (UK).⁷ On IMAT, the available pulsed (frequency of 10 Hz) neutron beam will be characterized by an intensity of 4×10^7 neutrons \times s⁻¹ \times cm⁻², and a cross-section of 20×20 cm² (wavelength range $0.7 \div 7.0$ Å).

The experimental setup of the adopted autofocusing system is described and 16 autofocusing algorithms among the more frequently adopted ones are compared against three different criteria of analysis. An overall score is assigned to each algorithm in order to select the most appropriate one. Finally, the procedure is described that is used to optimize the search for the maximum of the focus function.

II. THE IMAGING CAMERA

A number of different imaging cameras have been designed to meet different requirements and is currently em-

ployed at the various neutron imaging facilities around the world.^{8–12} However, different camera-boxes largely share a similar design because of the stringent requirements dictated by the neutron activation of the involved materials and by the possible radiation damages in the employed detectors. In designing and constructing the IMAT imaging camera, care has been taken in minimizing the amount of material located along the neutron path. A number of different field-of-views (FOVs) ranging from 5×5 cm² up to 20×20 cm² is covered, with different spatial resolutions. To cover such range of FOVs, we adopted commercially available fixed focus lens. The core of the imaging system consists of a Peltier cooled, gated and intensified CCD camera with the capability of “accumulate-on-chip” imaging. This last is needed to allow time-of-flight energy resolved imaging. An original lens holder, a mirror with two rotating degrees of freedom and the fully automated focusing system are the peculiar elements of the realized camera. Very few neutron imaging systems with remote focusing¹³ or self-focusing capabilities^{14,15} are described in the literature and in no case the focusing algorithm is detailed.

The imaging camera of IMAT (Figure 1) consists of a light-tight box, made of black anodized aluminium, coupled with the CCD camera. An interchangeable scintillator screen, placed in the front side of the box, produces an intensity modulated image of the neutrons transmitted through the sample. At present ⁶LiF/ZnS based scintillators are employed with thicknesses varying from 100 μm to 450 μm. Such scintillators, when interacting with neutrons, produce visible light with wavelengths in the 450–520 nm range. A glass mirror placed at 45° from the scintillator reflects the produced image towards the CCD camera. The mirror is mounted on a light aluminium frame that permits two orthogonal rotations in order to adjust the scintillator image on the lens axis.

A series of commercial optical lenses allows selecting among different fields of view, so obtaining different magnification ratios (to which different spatial resolutions correspond). The focal length of the lenses ranges from 50 mm to 135 mm and the *f*-number goes from 1.4 to 2.0. The working spatial resolution depends on both the lens focal length

^{a)}Author to whom correspondence should be addressed. Electronic mail: salvato@ipcf.cnr.it

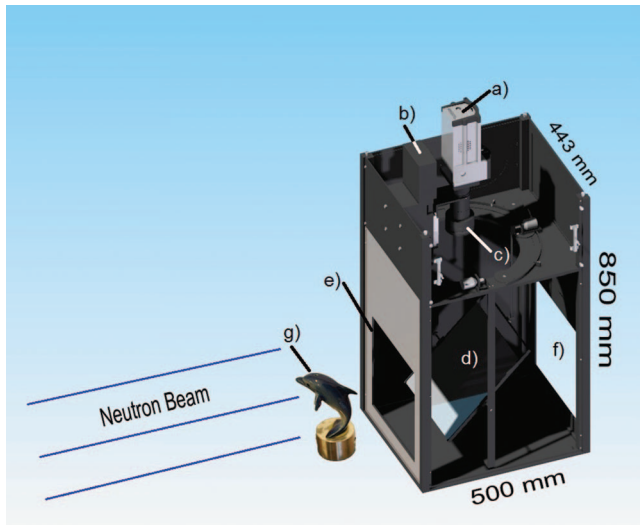


FIG. 1. The IMAT Camera: (a) CCD Camera; (b) Lens positioning linear stage; (c) Lens; (d) Mirror; (e) Front window (for placing scintillator screen, not shown); (f) Rear window (removed); (g) Sample.

and the spatial density of pixels of the adopted CCD. At IMAT, a $(13 \times 13 \text{ mm}^2)$ sensor will be adopted with 1024×1024 pixels (*Andor iStar 334t* see: <http://www.andor.com/>). It will achieve an optical resolution better than $100 \mu\text{m}$, when the 135 mm lens will be employed. We have chosen to use fixed focal lenses in order to maximize the f -number of the imaging system; in turns this means shorter exposure times and lower sample activation.

A lens holder, assembled on a remote controlled motorized linear stage (Figure 2) ensures a fast and easy way for changing lens. The same motorized stage is used for focusing.

The CCD that will be used at IMAT will be bought just before the utility will be ready so as to buy the best available model at that time. During the tests here reported we have used an *Andor iStar DH712* camera, equipped with a 512×512 pixel sensor (pixel size $24 \times 24 \mu\text{m}^2$). The camera has been coupled to the top of the box by means of an aluminum spacer. With such a choice the device is ready to adopt cameras with different CCD size (by substituting the spacer with a new one of suitable thickness). The total distance, L , between the CCD sensor and the scintillator screen is fixed to $L = 822 \text{ mm}$.

The motion range of the motorized linear stage (Newport M-ILS50PP, see: <http://www.newport.com/>) is about $\pm 25 \text{ mm}$

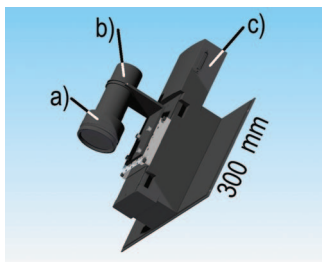


FIG. 2. Motorized linear stage with lens support: (a) Lens; (b) Extension Tube; (c) Lens focusing linear stage.

around its mechanical center, with accuracy of $0.5 \mu\text{m}$. Different extension tubes have been built, one for each lens, in order to obtain the focusing condition at about the same translator position, with no respect of the selected lens. The focus range to be explored with the linear stage is between -18.0 mm and -25.0 mm while the remaining range is used to change the lens.

A 3 mW laser diode (Global Laser Ltd., model *Cameo*) is mounted inside the light-tight box. It is equipped with a diffracting lens that splits the laser beam into a 13×13 dot matrix, which is projected onto the scintillator plane. The emission wavelength of the laser is 635 nm, well within both the scintillators reflectivity band and the CCD sensitivity window. The laser diode can be remotely switched on/off by a personal computer and the system accurate focusing can be quickly obtained (about 60 s) even when the beam is on so optimizing the beamline time.

Essentially to measure the focus of an image consists of computing quantities tied to the point spread function, i.e., of measuring the spread of a point-like light source at the sensor. By using a 13×13 dot pattern matrix it is possible to get, in the same image, a large number of such point-like sources in order to reduce the possible effect of noise largely. Furthermore, since the matrix is spread both horizontally and vertically, the focusing algorithms can weigh the defocusing in both directions. A 13×3 dot matrix is just one from many possible choices and a different number of dots could be used as well. We have tested our system with different dot patterns (printed on a paper sheet) without substantial differences.

III. EXPERIMENTAL PROCEDURE

For each lens, a series of images has been acquired with the lens position varying in the range $(-18.0 \div -25.0) \text{ mm}$. The focus metrics of the acquired image has been calculated with each of the considered algorithms and a “score” of the goodness of each algorithm has been calculated. Then, the algorithm with the best score has been selected and a golden-section search strategy has been implemented spanning the $(-18.0 \div -25.0) \text{ mm}$ search interval.

IV. AUTOFOCUS METRICS

In this work, the performances of 16 algorithms proposed for autofocus have been evaluated in order to select the best algorithm to be adopted at IMAT. In the following, we will list the tested algorithms.

A. Contrast based (F-0)

This algorithm¹⁶ calculates the absolute value of the difference between the brightness value of each pixel, $i(x, y)$, and that of first neighbours along the x and y axes,

$$G(x, y) = \sum_{j=x-1}^{x+1} |i(x, y) - i(j, y)| + \sum_{k=y-1}^{y+1} |i(x, y) - i(x, k)|. \quad (1)$$

The focus value is given by the sum of the square of $G(x, y)$ normalized to the number of pixels. H and W are the number of pixel along vertical and horizontal image directions, respectively,

$$F_{Contrast} = \frac{1}{H \cdot W} \sum_H \sum_W G(x, y)^2. \quad (2)$$

B. Squared Laplacian (F-1)

This algorithm convolves the image with the kernel

$$L_{xy}^2 = \begin{bmatrix} 0 & -1 & 0 \\ -1 & 4 & -1 \\ 0 & -1 & 0 \end{bmatrix} \quad (3)$$

to calculate the discrete Laplacian $C(x, y)$. The focus value is given by the sum of the squares of the convolution results normalized to the number of pixels

$$F_{Sq_Laplacian} = \frac{1}{H \cdot W} \sum_H \sum_W C(x, y)^2. \quad (4)$$

C. Generalized Laplacian (F-2)

This method is similar to the (F-1) but by assuming all neighbours to be at an equal distance then it includes the diagonals terms. The convolution kernel is

$$GL_{xy}^2 = \begin{bmatrix} 1 & 1 & 1 \\ 1 & -8 & 1 \\ 1 & 1 & 1 \end{bmatrix}. \quad (5)$$

Like the (F-1), the focus value is given by the sum of the squares of the convolution results normalized to the number of pixels

$$F_{Gen_Laplacian} = \frac{1}{H \cdot W} \sum_H \sum_W C(x, y)^2. \quad (6)$$

D. Thresholded absolute gradient (F-3)

This algorithm¹⁷ sums the absolute value of the first derivative greater than a given threshold θ ,

$$F_{Abs_Grad} = \sum_H \sum_W |i(x+1, y) - i(x, y)|, \quad (7)$$

where $|i(x+1, y) - i(x, y)| \geq \theta$.

E. Squared gradient (F-4)

This focus algorithm¹⁷ sums the square of the first derivative greater than θ ,

$$F_{Sq_Grad} = \sum_H \sum_W [i(x+1, y) - i(x, y)]^2, \quad (8)$$

where $[i(x+1, y) - i(x, y)]^2 \geq \theta$.

F. Brenner gradient (F-5)

The Brenner gradient algorithm¹⁸ computes the sum of the square of the difference between a pixel and its neighbour two pixels away when the difference is greater than θ ,

$$F_{Brenner} = \sum_H \sum_W [i(x+2, y) - i(x, y)]^2, \quad (9)$$

where $[i(x+2, y) - i(x, y)]^2 \geq \theta$.

G. Tenenbaum gradient (F-6)

This algorithm sums the square of the vector components obtained by the convolution of the image with the Sobel operator.^{19,20} The Sobel operator consists of a pair of 3×3 convolution kernels, G_x and G_y ,²¹

$$G_x = \begin{bmatrix} -1 & 0 & +1 \\ -2 & 0 & +2 \\ -1 & 0 & +1 \end{bmatrix}, \quad (10)$$

$$G_y = \begin{bmatrix} +1 & +2 & +1 \\ 0 & 0 & 0 \\ -1 & -2 & -1 \end{bmatrix}. \quad (11)$$

The convolution returns the components $S_x(x, y)$ and $S_y(x, y)$ of a vector. The value of focus is given by the following formula:

$$F_{Tenengrad} = \sum_H \sum_W S_x(x, y)^2 + S_y(x, y)^2. \quad (12)$$

H. Sum of modified Laplace (F-7)

This algorithm sums the absolute values of the vector components obtained by the convolution between the image and the 2D Laplacian operator,²²

$$F_{SML} = \sum_H \sum_W |L_x(x, y)| + |L_y(x, y)|, \quad (13)$$

where $L_x(x, y)$ and $L_y(x, y)$ are the components of the convolution, respectively, along the x and y axes of the image with the following kernels:

$$L_x = \begin{bmatrix} 0 & 0 & 0 \\ -1 & 2 & -1 \\ 0 & 0 & 0 \end{bmatrix}, \quad (14)$$

$$L_y = \begin{bmatrix} 0 & -1 & 0 \\ 0 & 2 & 0 \\ 0 & -1 & 0 \end{bmatrix}. \quad (15)$$

I. Energy Laplace (F-8)

The Energy Laplace algorithm²³ calculates the second derivative $C(x, y)$ applying the following kernel:

$$L = \begin{bmatrix} -1 & -4 & -1 \\ -4 & 20 & -4 \\ -1 & -4 & -1 \end{bmatrix}. \quad (16)$$

The output of the algorithm is computed by the following formula:

$$F_{En_Laplace} = \sum_H \sum_W C(x, y)^2. \quad (17)$$

J. Variance (F-9)

This algorithm^{13,24} sums the square of the difference between each pixel and the mean value μ of the grey level of the image and normalizes the sum to the number of the pixels of the image itself

$$F_{Variance} = \frac{1}{H \cdot W} \sum_H \sum_W [i(x, y) - \mu]^2. \quad (18)$$

K. Autocorrelation (F-10)

This algorithm computes the degree of correlation between neighbours pixels,^{25,26}

$$F_{AutoCorrelation} = \sum_H \sum_W [i(x, y) \cdot i(x + 1, y)] - \sum_H \sum_W [i(x, y) \cdot i(x + 2, y)]. \quad (19)$$

L. Standard deviation-based correlation (F-11)

In this algorithm, the degree of correlation is computed with respect to the standard deviation of the grey values of the image,^{25,26}

$$F_{StdDev_Corr} = \sum_H \sum_W [i(x, y) \cdot i(x + 1, y)] - H \cdot W \cdot \mu^2. \quad (20)$$

M. Range algorithm (F-12)

This algorithm computes the difference between the maximum and the minimum grey level intensity of a histogram of the image,²¹

$$F_{Range} = \max(h(i) > 0) - \min(h(i) > 0), \quad (21)$$

where $h(i)$ is a 256 bins histogram of the grey levels of the image.

N. Entropy algorithm (F-13)

Since in a focused image the diversity of grey levels is higher than that in a defocused one, this algorithm calculates the entropy value of the image in order to estimate how well it is focused.²⁷ By assuming $p_i = h(i)/H \cdot W$ is the probability

that a pixel has the grey level i , the output of this algorithm is given by the following formula:

$$F_{Entropy} = \sum_i p_i \log_2 p_i. \quad (22)$$

O. Prewitt gradient edge detection (F-14)

This algorithm¹⁵ is similar to the Tenenbaum gradient. The difference lies in a different kernel used for the convolution with the image. The kernel PG_x and PG_y are

$$PG_x = \begin{bmatrix} -1 & 0 & +1 \\ -1 & 0 & +1 \\ -1 & 0 & +1 \end{bmatrix}, \quad (23)$$

$$PG_y = \begin{bmatrix} +1 & +1 & +1 \\ 0 & 0 & 0 \\ -1 & -1 & -1 \end{bmatrix}. \quad (24)$$

The convolution returns the components $S_x(x, y)$ and $S_y(x, y)$ of a vector. The output of the algorithm is given by the following formula:

$$F_{Prewitt} = \sum_H \sum_W S_x(x, y)^2 + S_y(x, y)^2. \quad (25)$$

P. Energy of the image gradient (F-15)

This algorithm computes the sum of the square of the gradient components of the image,²⁸

$$F_{Energy_Grad} = \sum_H \sum_W [i(x - 1, y) - i(x + 1, y)]^2 + [i(x, y - 1) - i(x, y + 1)]^2. \quad (26)$$

V. ANALYSIS METHODOLOGY

To select the best focus algorithm three series of images that use three different lenses (50 mm, 85 mm, 135 mm) have been collected. The images have been acquired over a range of the linear stage position that goes from -25.0 mm to -18.0 mm, as imposed by the mechanical structure of the imaging system, with a $20 \mu\text{m}$ step. The target used to estimate the focus position is the 13×13 dots array projected by the laser diode. Figure 3 shows the focused images taken by using the 50 mm, 85 mm, and 135 mm lenses, respectively.

A data analysis has been carried out on the collected images in order to create, for each algorithm and for each lens, a focus curve as a function of the lens position. For the algorithms F-3, F-4, and F-5, the threshold values have been chosen equal to zero: different thresholds do not produce an appreciable difference.²⁹ Moreover, each obtained curve has been fitted with a Gaussian around its maximum. From these data, the best algorithm has been estimated by using an evaluation process performed in two successive steps: a qualitative analysis and a quantitative one.

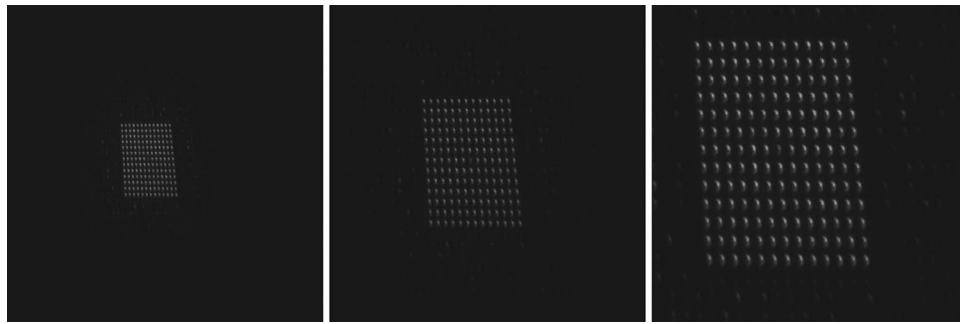


FIG. 3. Focused images taken using the 50 mm, 85 mm, and 135 mm lenses, respectively, from left to right.

A. Qualitative analysis

The qualitative analysis allows preliminarily to discard the algorithms that present a focus curve with at least one of these characteristics:

- local maxima comparable in intensity with the absolute maximum;
- strong asymmetry;
- very wide curve around the absolute maximum;
- curve with high noise;
- bad Gaussian fit.

The algorithms discarded by the qualitative analysis are listed below:

- Absolute gradient (F-3);
- Sum of modified Laplace (F-7);
- Range algorithm (F-12);
- Entropy algorithm (F-13).

In Table I, we report the reasons for which the algorithms were discarded.

B. Quantitative analysis

As a second step, a quantitative analysis has been carried out on the remaining algorithms. This analysis assigns an absolute score to each algorithm based on the evaluation of three key parameters:

- Difference between the position of the maximum of the curve and the center of the fitted Gaussian;
- Standard deviation of the fitted Gaussian;
- Adjusted R-square of the fit.

The adjusted R-square is defined as

$$\bar{R}^2 = 1 - \frac{RSS}{TSS} \frac{n-1}{n-p-1} = 1 - \frac{RSS}{TSS} \frac{df_{Total}}{df_{Error}}, \quad (27)$$

TABLE I. Discarding reasons for the various algorithms.

Discarded algorithms	Motivations				
	a	b	c	d	e
Absolute gradient (F-3)	x		x	x	
Sum of modified Laplace (F-7)	x	x	x	x	
Range algorithm F-13	x	x		x	x
Entropy algorithm F-14	x	x		x	x

where RSS is the residual sum of the square, TSS is the total sum of the square, n is the sample size, and p is the total number of regressors in the model.³⁰

The score is computed by using the Euclidean distance between these three parameters and their ideal values (0, 0, 1). The smaller the score, the better the algorithm performance. In our study, all the distances of the parameters from their ideal values are normalized in order to give the same weight to each one of these.

In the following tables (Tables II–IV), we show the scores of the algorithms analyzed quantitatively by using the 50-mm, 85-mm, and 135-mm lenses system respectively. Table V shows the overall score of the algorithms.

By following the results shown in Table V, the F-0 method has been selected for the IMAT camera focusing system.

In Figure 4, we illustrate the focus curves obtained from the selected algorithm in the range from -22 mm to -18 mm by using the three different lenses.

VI. THE SEARCH OF THE FOCUS

At the experimental beam-line, under working conditions, the maximum of the focus curve must be found by avoiding a time consuming exhaustive sequential search. We have then implemented a golden section search algorithm.^{31,32} Under the assumption that the focus curve is unimodal, this algorithm allows finding the maximum of a curve through a sequence of recursive steps, terminated by a stopping criterion. For each step, the algorithm needs to compute the value of the focus at a certain lens position, then the autofocus system moves the lens to that position, it takes a picture of the target (an exposure time of 3 ms is sufficient, by excluding vibrations effects) and it calculates the focus value. The search is terminated when the searching range becomes smaller than what would imply a circle of confusion equal to the pixel size. In our camera, the distance, L , between the CCD sensor and the scintillator screen is fixed (822 mm) and the pixel size will be $13 \mu\text{m}$ when the new camera will be available. The acceptable displacements are the ones shown in Table VI.

We have fixed the minimum search range at $20 \mu\text{m}$. The number of steps of the golden section search algorithm to reach the focus is not tied to the shape of the focus curve (provided it is unimodal) and it is fixed once the total search range and the minimum step are fixed, so it does

TABLE II. Score of the algorithms using the 50-mm lens system.

#	Algorithm name	xMax	Focus	Difference	Sigma	Adj. R-square	Score	Rank
F-0	Contrast based	-20.846	-20.85351	0.00751	0.10333	0.99429	0.6427	5
F-1	Squared Laplacian	-20.855	-20.86415	0.00915	0.07844	0.99872	0.50756	1
F-2	Generalized Laplacian	-20.855	-20.86283	0.00783	0.08441	0.99819	0.53245	3
F-4	Squared gradient	-20.855	-20.85962	0.00462	0.09314	0.99735	0.56846	4
F-5	Brenner gradient	-20.846	-20.85471	0.00871	0.10252	0.98878	0.65245	6
F-6	Tenenbaum gradient	-20.826	-20.84797	0.02197	0.11184	0.9868	0.82083	8
F-8	Energy Laplace	-20.855	-20.86355	0.00855	0.08144	0.99852	0.52015	2
F-9	Variance	-20.805	-20.84407	0.03907	0.12688	0.98323	1.1195	11
F-10	Autocorrelation	-20.826	-20.85172	0.02572	0.10843	0.97618	0.87511	10
F-11	Standard deviation-based correlation	-20.785	-20.83384	0.04884	0.16636	0.90552	1.73205	12
F-14	Prewitt gradient edge detection	-20.826	-20.84743	0.02143	0.11323	0.98645	0.82245	9
F-15	Energy of the image gradient	-20.826	-20.85028	0.02428	0.10626	0.98997	0.81633	7

not depend on the selected algorithm for measuring the focus goodness.

To show the performance of the self-focusing system, we may compare the obtained spatial resolution with the theoretical one. The field of view of the system when the 135 mm lens is used is about $50 \times 50 \text{ mm}^2$; this gives a maximum spatial resolution of 5 lines per mm when using our 512×512 pixel camera. In Figure 5, the image of a focused *1951 USAF Glass Slide Resolution Targets* from *Edmund Optics inc.* (see: <http://www.edmundoptics.com/testing->

[targets/test-targets/resolution-test-targets/1951-usaf-glass-slide-resolution-targets/1790](http://www.edmundoptics.com/testing-targets/test-targets/resolution-test-targets/1951-usaf-glass-slide-resolution-targets/1790)) is shown together with the enlarged versions of the central parts. The image has been acquired with the *Andor iStar DH712* camera endowed with a 512×512 pixel sensor and a *Nikon 135-mm f2.0* lens. The thickness of the glass slide on which the patterns are printed produces umbra into the white background by reducing the apparent image contrast. However, a resolution of 5.66 lines per mm can be recognized (element number 4 of the group number 2). This is very near to the maximum resolution that

TABLE III. Score of the algorithms using the 85-mm lens system.

#	Algorithm name	xMax	Focus	Difference	Sigma	Adj. R-Square	Score	Rank
F-0	Contrast based	-19.715	-19.71206	0.00294	0.13671	0.99785	0.87022	1
F-1	Squared Laplacian	-19.706	-19.69688	0.00912	0.11836	0.99483	1.43691	12
F-2	Generalized Laplacian	-19.706	-19.70013	0.00587	0.11959	0.99454	1.3116	10
F-4	Squared gradient	-19.715	-19.72100	0.00600	0.12573	0.99772	0.97536	2
F-5	Brenner gradient	-19.736	-19.72565	0.01035	0.13294	0.99770	1.29291	9
F-6	Tenenbaum gradient	-19.715	-19.72269	0.00769	0.13840	0.99731	1.15349	6
F-8	Energy Laplace	-19.706	-19.69854	0.00746	0.11899	0.99469	1.36477	11
F-9	Variance	-19.736	-19.73109	0.00491	0.16507	0.99913	1.00505	4
F-10	Autocorrelation	-19.736	-19.72807	0.00793	0.13688	0.99742	1.15464	7
F-11	Standard deviation-based correlation	-19.736	-19.73801	0.00201	0.18931	0.99882	1.04161	5
F-14	Prewitt gradient edge detection	-19.715	-19.72331	0.00831	0.13948	0.99734	1.1936	8
F-15	Energy of the image gradient	-19.715	-19.72015	0.00515	0.13522	0.99735	0.9969	3

TABLE IV. Score of the algorithms using the 135-mm lens system.

#	Algorithm name	xMax	Focus	Difference	Sigma	Adj. R-Square	Score	Rank
F-0	Contrast based	-19.018	-19.01718	0.00082	0.19988	0.99978	0.61601	1
F-1	Squared Laplacian	-18.968	-18.98038	0.01238	0.15951	0.99856	0.75055	2
F-2	Generalized Laplacian	-18.968	-18.98538	0.01738	0.16410	0.99854	0.94359	8
F-4	Squared gradient	-19.048	-19.06358	0.01558	0.21795	0.99976	0.97995	9
F-5	Brenner gradient	-19.088	-19.06621	0.02179	0.22724	0.99982	1.22009	11
F-6	Tenenbaum gradient	-19.028	-19.03446	0.00646	0.23511	0.99989	0.78169	3
F-8	Energy Laplace	-18.968	-18.98288	0.01488	0.16173	0.99855	0.84466	5
F-9	Variance	-19.048	-19.04925	0.00125	0.29425	0.99983	0.90697	7
F-10	Autocorrelation	-19.088	-19.06728	0.02072	0.23136	0.99983	1.18755	10
F-11	Standard deviation-based correlation	-19.028	-19.04612	0.01812	0.32508	0.99964	1.30049	12
F-14	Prewitt gradient edge detection	-19.028	-19.03564	0.00764	0.23792	0.99990	0.81153	4
F-15	Energy of the image gradient	-19.018	-19.02998	0.01198	0.22521	0.99974	0.88442	6

TABLE V. Overall score of the algorithms.

#	Algorithm name	Score	Rank
F-0	Contrast based	1.24492	1
F-1	Squared Laplacian	1.69872	7
F-2	Generalized Laplacian	1.70122	8
F-4	Squared gradient	1.49491	2
F-5	Brenner gradient	1.89366	11
F-6	Tenenbaum gradient	1.61720	4
F-8	Energy Laplace	1.68719	6
F-9	Variance	1.75671	9
F-10	Autocorrelation	1.87331	10
F-11	Standard deviation-based correlation	2.40338	12
F-14	Prewitt gradient edge detection	1.66123	5
F-15	Energy of the image gradient	1.56282	3

TABLE VI. Acceptable displacement of the lenses.

Lens (mm)	<i>f</i> -number	Acceptable displacement (μ m)
50	1.4	20
85	1.4	21
105	2.0	32
135	2.0	35

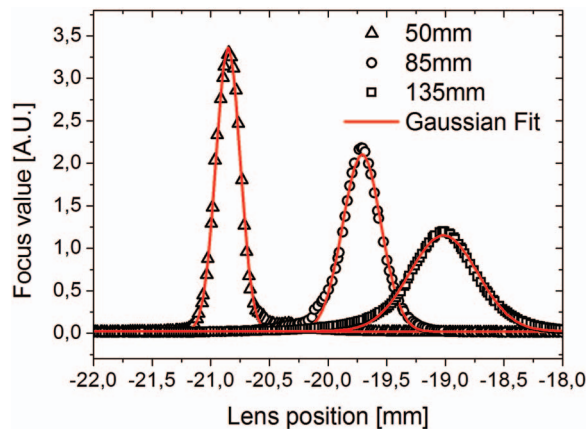


FIG. 4. Focus curves (normalized to the area) for the algorithm “Contrast Based” (F-0) with the 50 mm, 85 mm, and 135 mm lenses.

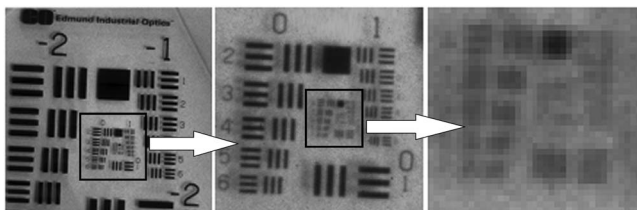


FIG. 5. Focused image of the 1951 USAF target acquired with a 135 mm lens. The central part of each image is shown magnified in going from left to right.

can be obtained with the available 512×512 pixel camera and the adopted optical magnification.

The software that is at present used to control all the operations of the camera, including the autofocus procedure, has been written in C++ (using *Microsoft Visual Studio*) by us and it is available to all users of the camera system. A software system integrated in the data acquisition system used at ISIS (SECI) will be ready within the due time.

VII. CONCLUSIONS

In this paper, the autofocus system of the imaging instrument used on IMAT has been presented. In the study here reported, we have compared 16 algorithms to select the best one. The algorithms have been evaluated by using both a qualitative analysis and a quantitative one. An overall score has been computed by taking into account three key parameters. The “contrast based” (F-0) algorithm, showing the best performance, has been selected for the autofocus system. The adopted setup together with the described autofocus system makes the camera a user-friendly imaging device allowing the beam time optimization.

ACKNOWLEDGMENTS

The Funding Agreement No. 06/20018 between CNR and STFC, concerning collaboration in mutual scientific research at the spallation neutron source ISIS (UK) is gratefully acknowledged.

Experiments at the ISIS Pulsed Neutron and Muon Source were supported by a beamtime allocation from the Science and Technology Facilities Council.

We are indebted to Dr. W. A. Kockelmann for the stimulating discussions.

We wish to thank D. Arigò, R. Caruso, G. Gismondo, D. Lupò, and G. Spinella of the CNR-IPCF for their great contribution on the mechanics and electronics of the camera.

¹G. Burca, J. A. James, W. Kockelmann, M. Fitzpatrick, S. Zhang, J. Hovind, and R. van Langh, *Nucl. Instrum. Methods Phys. Res. A* **651**, 229 (2011).

²D. Grolimund, D. Berger, S. Bolliger Schreyer *et al.*, *J. Anal. At. Spectrom.* **26**, 1012 (2011).

³J. J. Rant, Z. Milic, P. Turk, and I. Lengar, “Application of contemporary non-destructive testing in engineering,” in *Proceedings of the 8th International Conference of the Slovenian Society for Non Destructive Testing*, 2005, pp. 181–188 (<http://www.ndt.net/article/ndt-slovenia2005/PAPERS/21-NDTP05-80.pdf>).

⁴F. Salvemini, F. Grazi, S. Peetermans, F. Civita, R. Franci, S. Hartmann, E. Lehmann, and M. Zoppi, *J. Anal. At. Spectrom.* **27**, 1494–1501 (2012).

⁵F. Kim, D. Penumadu, and D. Hussey, *J. Geotech. Geoenviron. Eng.* **138**, 147 (2012).

⁶S. Pierret, A. Evans, A. M. Paradowska, and M. Fitzpatrick, *NDT & E Int.* **45**, 39 (2012).

⁷W. Kockelmann, S. Y. Zhang, J. F. Kelleher, J. B. Nightingale, G. Burca, and J. A. James, *Phys. Procedia* **43**, 100 (2013), see also <http://www.isis.stfc.ac.uk/>.

⁸L. Bartoli, F. Aliotta, F. Grazi, G. Salvato, C. S. Vasi, and M. Zoppi, “Test measurements with a new neutron imaging alignment camera at ISIS,” *Nucl. Instrum. Methods Phys. Res. A* **595**, 643–646 (2008).

⁹G. Frei, E. H. Lehmann, D. Mannes, and P. Boillat, “The neutron microtomography setup at PSI and its use for research purposes and engineering applications,” *Nucl. Instrum. Methods Phys. Res. A* **605**, 111–114 (2009).

- ¹⁰M. Segawa, T. Kai, T. Sakai, M. Ooi, and M. Kureta, "Development of a high-speed camera system for neutron imaging at a pulsed neutron source," *Nucl. Instrum. Methods Phys. Res. A* **697**, 77–83 (2013).
- ¹¹T. E. McDonald, Jr., T. O. Brun, T. N. Claytor, E. H. Farnum, G. L. Greene, and C. Morris, "Time-gated energy-selected cold neutron radiography," *Nucl. Instrum. Methods Phys. Res. A* **424**, 235–241 (1999).
- ¹²A. Sinha, "Development of three dimensional neutron tomography system and its applications," *Rev. Sci. Instrum.* **71**, 1455 (2000).
- ¹³J. S. Brenizer, H. Berger, K. M. Gibbs, P. Mengers, C. T. Stebbings, D. Polansky, and D. J. Rogerson, "Development of a new electronic neutron imaging system," *Nucl. Instrum. Methods Phys. Res. A* **424**, 9–14 (1999).
- ¹⁴R. Lewandowski, L. Caon, and D. Turkoglu, "Noise evaluation of a digital neutron imaging device," *Nucl. Instrum. Methods Phys. Res. A* **674**, 46–50 (2012).
- ¹⁵D. Turkoglu, L. Cao, and R. Lewandowski, "A low-cost neutron radiography device," *Phys. Procedia* **43**, 54–65 (2013).
- ¹⁶X. Xu, Y. Wang, J. Tang, X. Zhang, and X. Liu, *Sensors* **11**, 8281 (2011).
- ¹⁷A. Santos, C. O. Solórzano, J. J. Vaquero, J. M. Peña, N. Malpica, and F. Pozo, *J. Microsc.* **188**, 264 (1997).
- ¹⁸J. F. Brenner, B. S. Dew, J. B. Horton, J. B. King, P. W. Neirath, and W. D. Sellers, *J. Histochem. Cytochem.* **24**, 100 (1976).
- ¹⁹T. Yeo, S. O. Jayasooriah, and R. Sinniah, *Image Vis. Comput.* **11**, 629 (1993).
- ²⁰E. Krotkov, *Int. J. Comput. Vis.* **1**, 223 (1988).
- ²¹R. C. Gonzalez and P. Wintz, *Digital Image Processing*, 2nd ed. (Addison-Wesley, Reading, MA, 1987).
- ²²S. K. Nayar and Y. Nakagawa, *IEEE Trans. Pattern Anal. Mach. Intell.* **16**, 824 (1994).
- ²³M. Subbarao, T. S. Choi, and A. Nikzad, *J. Opt. Eng.* **32**, 2824 (1993).
- ²⁴F. Groen, I. T. Young, and G. Lighthart, *Cytometry* **6**, 81 (1985).
- ²⁵D. Vollath, *J. Microsc.* **147**, 279 (1987).
- ²⁶D. Vollath, *J. Microsc.* **151**, 133 (1988).
- ²⁷L. Firestone, K. Cook, K. Culp, N. Talsania, and K. Preston, *Cytometry* **12**, 195 (1991).
- ²⁸M. Faundez-Zanuy, J. Mekyska, and V. Espinosa-Duró, *Pattern Recog. Lett.* **32**, 1548 (2011).
- ²⁹Y. Sun, S. Duthaler, and B. J. Nelson, *Microsc. Res. Tech.* **65**, 139 (2004).
- ³⁰See <http://www.originlab.com/www/helponline/Origin/en/origin.htm> for Origin 8 Manual.
- ³¹J. Kiefer, *Proc. Am. Math. Soc.* **4**, 502 (1953).
- ³²W. H. Press, S. A. Teukolsky, W. T. Vetterling, and B. P. Flannery, *Numerical Recipes in C: The Art of Scientific Computing*, 2nd ed. (Cambridge University Press, Cambridge, England, 1992), pp. 397–400.